The Southeast Indian Ridge: A Hotspot for Cross-Frontal Exchange

ALEXIS JOHNSON EXLEY,[a] KATHLEEN DONOHUE,[a] AND D. RANDOLPH WATTS[a]

[a] *The University of Rhode Island, Kingston, Rhode Island*

(Manuscript received 9 March 2024, in final form 31 January 2025, accepted 17 February 2025)

ABSTRACT: Cross-frontal exchange facilitated by mesoscale eddies in the lee of major topographic features of the Southern Ocean is fundamental to the global overturning circulation. Despite the outsize importance for meridional heat flux, we lack an accurate estimation of fluxes across the Antarctic Circumpolar Current (ACC) due to the challenges of observing mesoscale eddy fluctuations on the temporal and spatial scales required. Here, 12 years of Argo data are used to observe patterns of cross-frontal exchange in the Southeast Indian Ridge system, a relatively underobserved region, known to be a hotspot of exchange. Spice variance along ACC streamlines is used as a proxy for cross-frontal exchange. Elevated exchange is observed downstream of the ridge system in nearly every streamline and is particularly prominent in the core of the ACC. Notably, exchange peaks progressively downstream at each poleward streamline suggesting a systematic north-to-south handoff across nearly the full breadth of the ACC. Employing a mixing length framework, lateral stirring is parameterized as an eddy diffusivity on the isopycnal of peak exchange. We find a highly localized pattern of diffusivity, peaking between the crest and trough of the first standing meander in the lee of the ridge system. Spatially, this diffusivity pattern correlates with an along-stream increase in eddy kinetic energy. Along-stream vertical wavenumber spectra of spice anomaly profiles indicate that the vertical scales of intrusions, which are initially large (approximately 800 m), rapidly evolve downstream to smaller wavenumbers (100–300 m) presumably in response to intense vertical shear and filamentation.

KEYWORDS: Diffusion; Eddies; Mesoscale processes; Mixing; Orographic effects

1. Introduction

The meridional overturning circulation plays a fundamental role in our climate system by transporting heat, carbon, and other biogeochemical properties around the globe (Bryan and Lewis 1979). While buoyancy loss and convection in the North Atlantic have traditionally been thought of as the primary driver, the return arm in the Southern Ocean plays an equally important role. The outcropping of isopycnals within the Antarctic Circumpolar Current (ACC) ventilates deep, carbon-rich waters to the surface ocean and, through the conversion to bottom and intermediate waters, compensates the sinking in the North Atlantic (Marshall and Speer 2012).

The Southern Ocean overturning circulation is traditionally described in a two-dimensional, zonally averaged framework comprised of two distinct overturning cells (Deacon 1937; Speer et al. 2000; Sloyan and Rintoul 2001). North Atlantic Deep Water spreads southward along isopycnals and transforms into two classes of Circumpolar Deep Water (CDW). Lower CDW outcrops near Antarctica, south of the ACC, where buoyancy forces and brine rejection during sea ice formation convert this water mass into denser Antarctic Bottom Water. Once formed, these deep waters are exported to the global abyssal ocean forming the lower cell of the Southern Ocean overturning. Within the ACC, energetic wind-driven upwelling brings upper CDW to the surface layer where interaction with the atmosphere transforms this water mass into less dense Antarctic Intermediate Water and Subantarctic Mode Water. Ekman transport moves these surface waters northward, forming the upper cell of the Southern Ocean overturning.

Fundamental to the zonally averaged view of the Southern Ocean overturning circulation is the role of mesoscale eddies and the associated poleward transport of fluid. Within the ACC, wind-driven Ekman transport steepens poleward shoaling isopycnals until they become baroclinically unstable. Drawing from available potential energy, an opposing eddy-driven circulation acts to slump isopycnals and counterbalance the wind-induced transport. Below the surface layer, this mesoscale eddy field facilitates the poleward and upward transfer of water which would otherwise require unrealistically large vertical mixing (Lumpkin and Speer 2007; Marshall and Speer 2012). These eddies are therefore critical to the Southern Ocean mass budget and to move heat, carbon, nutrients, and other properties across the strong jets of the ACC which would typically act to impede poleward flux. The meridional transport of mass across the ACC thus couples baroclinic eddies to the Southern Ocean overturning circulation and plays a significant role in establishing the strength and structure of the system.

Though this zonally averaged view of the ACC has been indispensable in shaping our understanding of the Southern Ocean's role in the global overturning circulation, it is a simplified schematic of a zonally asymmetric system. Theoretical and experimental studies have shown that cross-frontal exchange due to eddy fluxes across ACC fronts is inhibited in most regions of the Southern Ocean due to suppression of across-stream eddy mixing length scales (Abernathey et al. 2010; Ferrari and Nikurashin 2010; Naveira Garabato et al. 2011; Sallée et al. 2008). This characteristic mixing length suppression breaks down, however, in a few critical locations

Corresponding author: Alexis Johnson Exley, ajohnson1@uri.edu

DOI: 10.1175/JPO-D-24-0037.1

© 2025 American Meteorological Society. This published article is licensed under the terms of the default AMS reuse license. For information regarding reuse of this content and general copyright information, consult the AMS Copyright Policy (www.ametsoc.org/PUBSReuseLicenses).

Brought to you by MBL/WHOI Library | Unauthenticated | Downloaded 05/27/25 11:50 AM UTC

around the Southern Ocean. Sharp standing meanders of the ACC are established as fronts navigate around major topographic ridge systems of the Southern Ocean and are held stationary by the background flow (Abernathey and Cessi 2014). In these regions, flow transitions from a parallel, zonal regime to that of an unstable, energetic meandering one. This results in "leaky jet segments" (Naveira Garabato et al. 2011) and subsequent exchange of properties across frontal structures of the ACC.

The transition between flow regimes is initiated as the ACC propagates off major ridge systems of the Southern Ocean (Youngs et al. 2017). While confined to the ridge, jets converge and isopycnals steepen and are simultaneously stabilized by the bathymetry. Downstream, flow deflects poleward, becomes unstable, and potential energy stored in the steepened isopycnals is released, generating a mesoscale eddy field, meandering of the flow, and the merging and splitting of jets (Thompson and Garabato 2014; Rintoul 2018). Eddies facilitate a preferentially poleward cross-frontal exchange (Dufour et al. 2015) resulting in a net poleward heat transport (Meijer et al. 2022) and an along-stream increase in tracer variability. Around the circumpolar ACC path, this enhanced exchange is localized in six narrow regions in the lee of major topographic features of the Southern Ocean (Sallée et al. 2008; Sallée et al. 2011; Thompson and Sallée 2012). Modeling work has shown the resulting interior circulation follows an upward spiral such that fluid moves further poleward and closer to the surface at each progressively downstream topographic hotspot, until it becomes entrained within the Weddell or Ross Seas (Tamsitt et al. 2017). Satellite-based observations substantiate this idea, showing that maximum exchange occurs along different streamlines at each topographic hotspot illustrating a handoff of fluid and heat from one front to another along the path of the ACC (Foppert et al. 2017).

Occurring in regions that make up only a small fraction of the total zonal extent of the ACC, namely, around 20%, these zonally asymmetric processes contribute disproportionately to the magnitude of meridional heat transport, ventilation of the deep, and the Southern Ocean carbon pump. Studies show that the vast majority (up to 75%) of total ACC cross-frontal particle transport (Thompson and Sallée 2012; Tamsitt et al. 2017) and southward temperature transport due to eddy heat flux (Dufour et al. 2015; Peña-Molino et al. 2014; Foppert et al. 2017) is concentrated downstream from topography. Additionally, general circulation models coupled to active biogeochemistry simulations suggest that around 70% of the total amount of carbon dioxide upwelling to the surface in the Southern Ocean occurs within these hotspots (Brady et al. 2021). These asymmetries highlight the need to account for the three-dimensionality of the Southern Ocean overturning circulation within ocean and climate models.

In coarse, noneddy-permitting ocean and coupled atmospheric models, the eddy-driven transport of tracers is not explicitly resolved and, alternatively, is parameterized as an eddy diffusivity κ. This diffusive parameterization quantifies the effectiveness of eddies to homogenize thickness gradients (Gent and Mcwilliams 1990) by relating the eddy-induced flux of a tracer to the mean background tracer gradient. Significant uncertainties within these models pertain to the magnitude, as well as the spatial and temporal variability of κ. An accurate quantification of eddy diffusivity in these models remains a formidable challenge, in part, because obtaining meaningful observational-based flux estimates requires high-resolution measurements over significant spatial and temporal scales.

While a number of studies have attempted to estimate Southern Ocean eddy diffusivities from satellite measurements (e.g., Sallée et al. 2008), technological advancements and a significant increase in observations have allowed for depth-dependent estimates at higher resolutions. These estimates are derived from float and/or tracer dispersion studies, such as the Diapycnal and Isopycnal Mixing Experiment (Klocker et al. 2012; LaCasce et al. 2014; Tulloch et al. 2014; Balwada et al. 2016), and observed hydrographic variability measured from CTD profiles. This work builds on two previous studies that have used hydrographic variability to obtain estimates of eddy diffusivity using a mixing length framework. The first is Cole et al. (2015) who use the global Argo array to bin profiles into 3° boxes to show that eddy diffusivity varies significantly around the globe and in depth. While this novel methodology advanced our understanding of global diffusivity patterns, the resolution is too low to quantify Southern Ocean eddy stirring confined to small regions downstream from topography. The second study, Naveira Garabato et al. (2011), characterizes the vertical and horizontal structure of eddy diffusivity using a set of repeat hydrographic sections across the ACC. They identify distinct mixing regimes associated with stationary meanders and large eddy diffusivities coinciding in the vertical with large isopycnal potential vorticity gradients. That work is benefited by higher-resolution observations but is confined to these synoptic CTD sections. Here, we aim to maintain the resolution of Naveira Garabato et al. (2011) while moving away from repeat sections by adopting a similar Argo float methodology developed by Cole et al. (2015).

In this study, Argo float profiles are mapped to geopotential streamlines of the ACC to characterize the stirring of physical fluid properties across fronts of the ACC and estimate patterns of eddy diffusivity in the lee of the Southeast Indian Ridge (SEIR) (Fig. 1). The physical stirring process is termed cross-frontal exchange and is qualitatively defined as the tracer variance measured from Argo profiles. This tracer variance is then used in conjunction with numerical model output to quantify eddy diffusivity using a mixing length framework. We focus on the SEIR region for a number of reasons. It has been shown to be a hotspot for cross-frontal exchange (Sallée et al. 2011; Thompson and Sallée 2012; Thompson and Garabato 2014; Meijer et al. 2022) and eddy heat flux (Phillips and Rintoul 2000; Foppert et al. 2017) due to the northward deflection and subsequent confluence of nearly all ACC streamlines as they navigate the northwest-to-southeast step-like geometry of the ridge system (Fig. 1). It is also one of the few locations in the ACC where observations suggest the magnitude of eddy heat flux has increased over time in concert with the increasing wind stress (Foppert et al. 2017). Finally, eddy fluxes in the lee of this ridge system are relatively understudied and underobserved in comparison to

Brought to you by MBL/WHOI Library | Unauthenticated | Downloaded 05/27/25 11:50 AM UTC

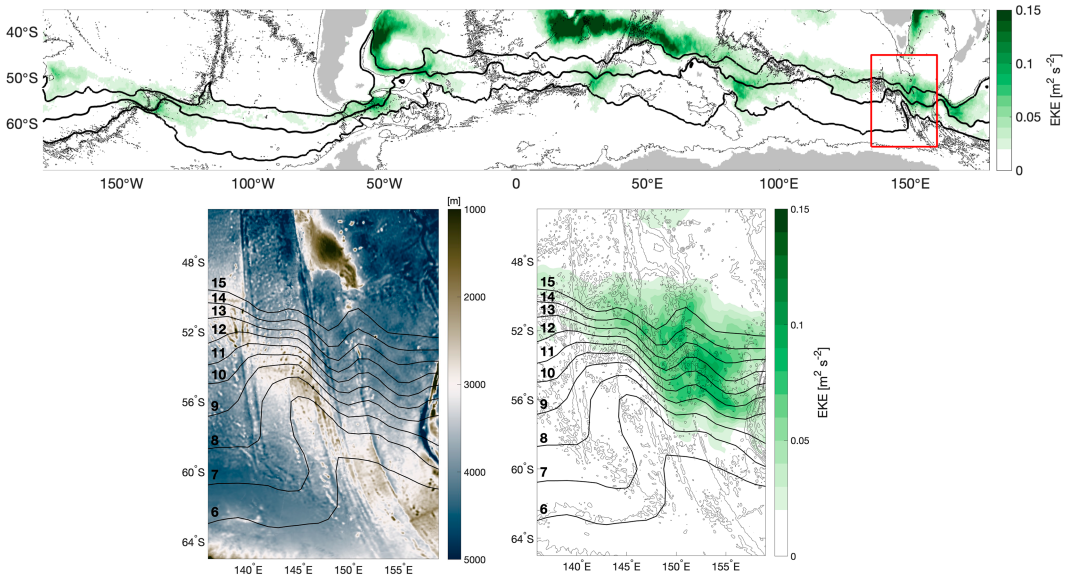


FIG. 1. (top) Sea surface eddy kinetic energy overlaid on 3000-m bathymetry contours. Sea surface height contours (solid black) correspond to the Subantarctic Front, Polar Front, and Southern ACC Front (north–south, respectively). The red box indicates the SEIR region. (bottom) Argo-derived temporal mean geopotential height contours (vertically integrated specific volume from 1800 to 150 m) overlaid on bathymetry of the (left) SEIR region and (right) eddy kinetic energy. Geopotential contours are labeled and span values from 6 $m^2\ s^{-2}$ (southernmost streamline) to 15 $m^2\ s^{-2}$ (northernmost streamline).

other topographic regions of the Southern Ocean such as Drake Passage.

The datasets used in this study are described in section 2. Section 3 explains in detail the methodologies developed to map Argo profiles to geopotential streamlines and the mixing length framework used to estimate eddy diffusivity. Section 4 details both horizontal and vertical patterns of cross-frontal exchange in the SEIR region and illustrates patterns of horizontal eddy diffusivity. In section 5, observed eddy diffusivities are compared against previous studies, and patterns are examined in relation to known proxies of eddy mixing and baroclinic instabilities. We also propose an along-stream evolution of cross-frontal intrusions that reduces the vertical scale of anomalies after exchange across fronts. We conclude with a summary in section 6.

2. Data

a. *Argo profiling floats*

Argo floats typically profile the upper 2000 m of the ocean, sampling physical properties of the water column at a time interval of 2–10 days (Wong et al. 2020). For this study, we used 12 years of Argo data from the SEIR region of the Southern Ocean, an area defined as 65°–45°S, 135°–160°E (Fig. 1). Delayed-mode data with "good data" quality control flags were obtained using the EuroArgo Selection Tool (Argo 2000). During processing, profiles that do not reach a minimum of 1800 m, contain missing data, or exceed a vertical resolution of 200 m anywhere in the profile are removed. In total, 22 689 profiles from 594 floats sampling between the years 2010 through 2022 comprise the final dataset.

All the profiles in the SEIR region are interpolated onto an even 5-m vertical resolution pressure grid. A mixed-layer depth is calculated for each profile using the Holte and Talley (2009) Argo mixed-layer depth algorithm. This algorithm determines the mixed-layer depth using a seasonal thermocline fit or by identifying intrusions at the base of the mixed layer, depending on if the profile is flagged as a summer or winter profile, respectively. If either method fails, mixed-layer depth is calculated using a density threshold or a density gradient method. Profiles are then mapped into density space by interpolating onto a density grid with 0.005 kg m^{-3} vertical resolution. The density at the predetermined mixed-layer depth is retained as the mixed-layer density.

Each profile of Conservative Temperature and Absolute Salinity is then converted to a spice profile following McDougall and Krzysik (2015). Spice is a dynamically passive thermodynamic variable that is conserved following the fluid parcel with isolines orthogonal to potential density contours. It is a property that quantifies how water properties change along an isopycnal and is therefore the best available measure of along-isopycnal water-mass variability and isopycnal mixing. Additionally, a geopotential height for each Argo profile is calculated by vertically integrating the specific volume anomaly from 1800 to 150 m (Pond and Pickard 1983). Argo profiles are mapped into 1° × 1° boxes to generate mean geopotential streamlines overlaid on Fig. 1.

b. *GLORYS*

The Global Ocean Physics Reanalysis (GLORYS) product is an eddy-resolving 1/12° horizontal resolution global reanalysis.

Brought to you by MBL/WHOI Library | Unauthenticated | Downloaded 05/27/25 11:50 AM UTC

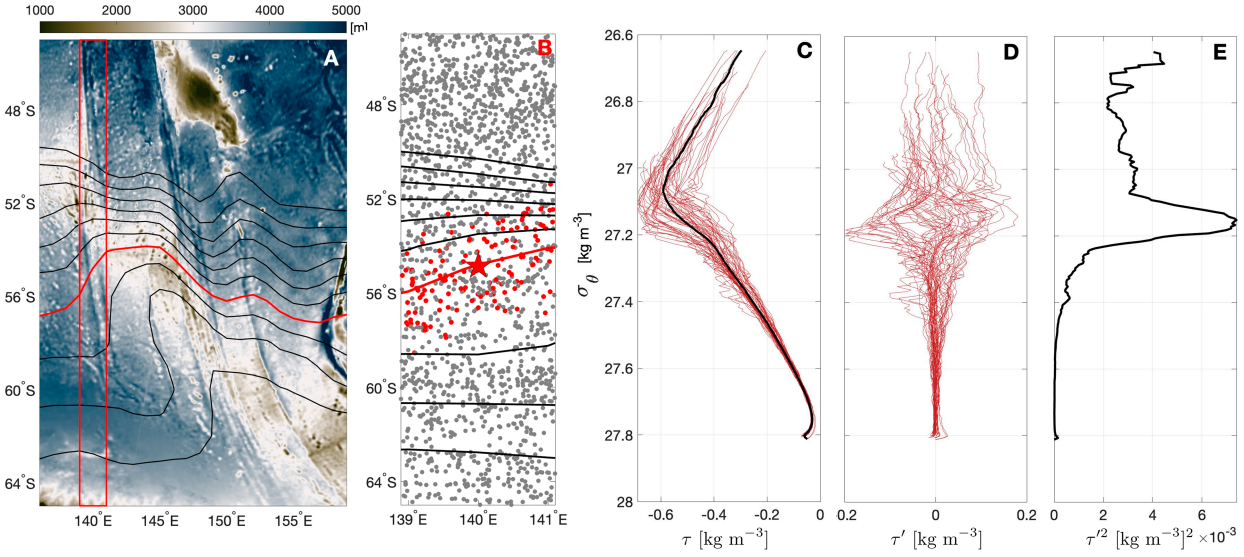


FIG. 2. (a) ACC geopotential streamlines overlaid on bathymetry with the Polar Front streamline in red and the cutout in (b) highlighted. (b) Sliding box with the location of all Argo profiles in that box. Red dots indicate the Argo profiles with geopotential height between 8.5 and 9.5 m^2 s^{-2} to be mapped to the Polar Front (geopotential 9 m^2 s^{-2}). (c) A subset of the spice profiles at 140°E on the 9 m^2 s^{-2} streamline in potential density space indicated by the red dots in (b). The mean spice profile is in black. (d) Spice anomaly profiles and (e) the corresponding spice anomaly variance profile.

Here, we use both the monthly mean fields (1993–2023) and a year of daily mean fields (2020). It assimilates Argo profiling floats and sea surface satellite altimetry. Both mean and daily temperature, salinity, and current velocity fields are obtained from Copernicus Marine Services. Original files are displayed on 50 vertical pressure levels and interpolated onto a density grid to match that of the Argo data. Geopotential and spice fields are calculated following the same procedures as for the Argo profiles (section 2a).

3. Methods

a. Argo mapping methodology

Methods closely follow those developed by Cole et al. (2015) who provide a global estimate of horizontal diffusivity using geographically binned tracer variance and a mixing length framework. In this study, however, we are motivated to average in an ACC coordinate system so profiles are organized by geopotential height values which closely represent the mean streamlines of the ACC. This allows for a detailed investigation of alongfront variability. Tracer variance is calculated on geopotential height contours from 6 through 15 m^2 s^{-2} as these represent the streamlines that successfully navigate Drake Passage. The Polar Front is represented by the 9 m^2 s^{-2} geopotential height contour and is used to illustrate the Argo mapping methodology described below (Fig. 2a: red contour).

A spice profile and geopotential height value are calculated for each Argo profile. Profiles are then "mapped" to every 1° of longitude along each geopotential height contour. This is similar to the binning technique used by Cole et al. (2015), but here it is adapted to an along-streamline coordinate system. This is described below and illustrated schematically in Fig. 2. The goal is to obtain a collection of Argo profiles at every longitudinal degree point, along each streamline. First, a 2° longitudinal window is defined from the larger domain. An example of one of these 2° windows is illustrated as the red rectangle in Fig. 2a. In this example, the longitudinal window spans 139°–141°E. Next, a subset of Argo profiles is defined, considering only those with a location within our 2° longitudinal window. The subset of profiles, spanning the 2° window, is enlarged in Fig. 2b.

Argo profiles from the subset are then assigned to the central longitude of each geopotential height contour within the 2° window. To accomplish this, we consider the calculated geopotential height value for each individual Argo profile. The profiles with a geopotential within ±0.5 m^2 s^{-2} of each contour are assigned to the central longitude along that specified contour. This is again illustrated schematically in Fig. 2b. In this example, the goal is to create a collection of Argo profiles that will be assigned to the 140°E longitude point along the Polar Front, which has a geopotential height value of 9 m^2 s^{-2}. From the original subset of Argo profiles, we find those with a geopotential height value of 8.5–9.5 m^2 s^{-2} (Fig. 2b: red circles). That collection of profiles is then assigned to the 140°E (Fig. 2b: red star) longitude point along the Polar Front. This process is then repeated for the next geopotential height contour by finding all Argo profiles with a geopotential height value of 9.5–10.5 m^2 s^{-2}. That new collection of Argo profiles is assigned to the 140°E longitude point along the streamline represented by the 10 m^2 s^{-2} geopotential height contour. This is again repeated for each geopotential height contour within the 2° window.

Once a collection of profiles has been obtained for each geopotential height contour at the 140°E longitude point, the

Brought to you by MBL/WHOI Library | Unauthenticated | Downloaded 05/27/25 11:50 AM UTC

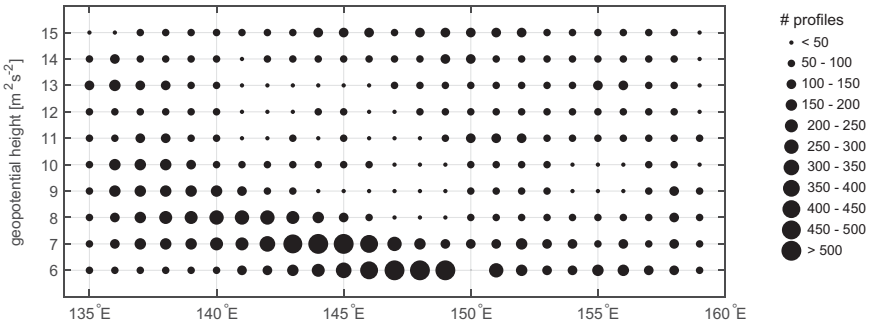


FIG. 3. Number of profiles mapped to every 1° longitude point along geopotential contours.

2° window is slid to the east by 1°, and the process is repeated, starting with a new subset of Argo profiles. In this example, the new subset will now contain all Argo profiles with a longitude between 140° and 142°E, and profiles will be assigned to the central longitude point at 141°E. The overlap that results from the sliding 2° subset provides a reasonable level of smoothing while increasing the number of profiles mapped to each point, thereby increasing the degrees of freedom and our confidence in the result. The result of this "mapping" methodology is a unique set of Argo profiles at every 1° longitude point along each geopotential height contour. The number of profiles mapped to each longitudinal point ranges from a minimum of around 50 to well over 200 profiles (Fig. 3).

b. *Estimating cross-frontal exchange*

A qualitative estimate of cross-frontal exchange is then diagnosed by calculating the spice anomaly variance of the collection of profiles mapped to every longitudinal degree point along each geopotential height streamline (Fig. 2c: red profiles). To accomplish this, the mixed layer is first removed from each profile. The following steps occur individually with the collection of profiles at each longitude point along every streamline. In density space, a mean spice profile (Fig. 2c: black profile) is calculated from the collection of profiles obtained from the mapping methodology detailed above. A spice anomaly profile is calculated as the difference, at each density layer, between the original spice profile and the mean (Fig. 2d). The total variance and variance profile of the collection of spice anomaly profiles are then calculated (Fig. 2e). The end product is a unique value of tracer variance (and a variance profile) at every 1° longitude along each geopotential streamline. This tracer variance illustrates the relative degree of influence from adjacent water masses at a given location and is therefore representative of exchange across ACC fronts. Therefore, while we cannot use this diagnostic to explicitly quantify the degree of exchange at every point, it is a robust qualitative and comparative measure of cross-frontal exchange.

c. *Estimating horizontal eddy diffusivity*

Our analysis of cross-frontal exchange lends itself to a local, high-resolution, hydrographic-variability-based estimate of eddy diffusivity within a mixing length framework (Fig. 7). This work builds upon the hydrographic variability-based approach from Naveira Garabato et al. (2011) and again closely follows the procedure of Cole et al. (2015). Within the mixing length framework, cross-stream eddy diffusivity relates the background mean tracer field to the observed departure from that mean as $\kappa = c_e U_e L_{\text{mix}}$, where L_{mix} is the eddy mixing length scale and U_e is the eddy velocity scale given as

$$L_{\text{mix}} = \frac{\tau_{\text{rms}}}{|\nabla \tau_m|}, \tag{1}$$

$$U_e(t) = \sqrt{\langle [U(t) - U_m]^2 + [V(t) - V_m]^2 \rangle}. \tag{2}$$

Here, τ_{rms} is the root-mean-square of the spice anomaly calculated from the Argo profiles and $|\nabla \tau_m|$ is the mean background spice gradient averaged over all years from the GLORYS product (1993–2023). The eddy velocity scale $U_e(t)$ is calculated as a time series using a year (2020) of daily mean GLORYS output, $U(t)$ and $V(t)$, and the mean background velocity, U_m and V_m, averaged over all years of the GLORYS product. The daily $U_e(t)$ fields are then averaged over the year to get a time mean U_e field. The mixing coefficient c_e can roughly range from 0.01 to 0.4 in numerical simulations; however, due to the uncertainty in magnitude, we choose to largely omit it from our analysis and focus on κc_e^{-1} as the diffusivity parameter. For each geopotential streamline, L_{mix}, U_e, and the resulting diffusivity product are calculated on the isopycnal (± 0.05 kg m^{-3}) of peak variance as identified from Fig. 6.

4. Results

a. *Cross-frontal exchange*

Using the qualitative measure, spice variance, as a proxy for cross-frontal exchange, along streamline patterns of eddy activity are identified in the SEIR region of the Southern Ocean. To illustrate these patterns and highlight the impact of topography on cross-frontal exchange, temperature and salinity diagrams are compared against spice anomaly profiles in these locations along the Polar Front representative of 1) a region upstream from topography (140°E), 2) at the topography (146°), and 3) downstream from topography (152°) (Fig. 4).

Upstream from the ridge system, where the flow is largely zonal and eddy fluxes are suppressed, relatively weak cross-

Brought to you by MBL/WHOI Library | Unauthenticated | Downloaded 05/27/25 11:50 AM UTC

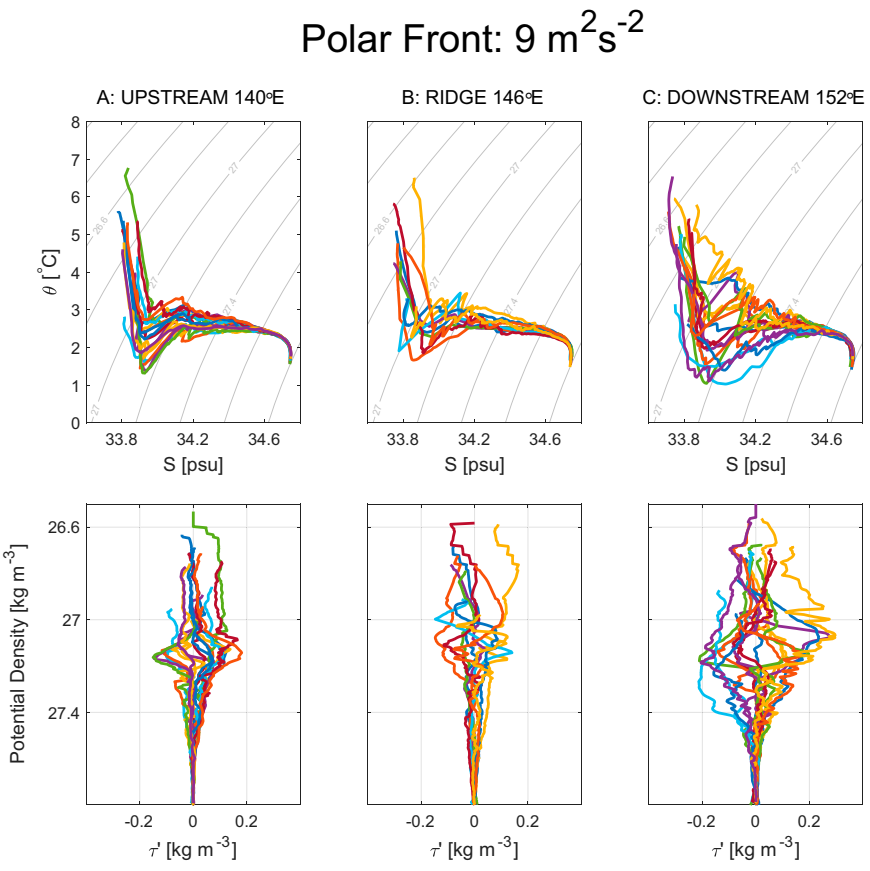


FIG. 4. (top) Potential temperature and salinity diagrams from points (a) 140°E, (b) 146°E, and (c) 152°E along the Polar Front (9 m^2 s^{-2}). These points are characteristic of the upstream, topographic, and downstream regions, respectively. Potential density is contoured and labeled in the background. (bottom) Spice anomaly profiles from the same points in potential density space. Spice anomaly profiles correspond to the same locations as the top panels. The mixed layer is removed from all profiles.

frontal exchange is expected. In this upstream region (Fig. 4: column a), temperature and salinity profiles span a relatively small range on isopycnals. Corresponding spice anomaly profiles exhibit some variability near the surface, a peak below the 1027.0 kg m^{-3} isopycnal, and a decrease in variability with depth. On the topographic ridge (Fig. 4: column b), patterns largely reflect the upstream region illustrating the stabilizing effect the bathymetry has on the flow. In contrast, downstream from the ridge, as the flow becomes energetic and the mesoscale eddy field facilitates cross-frontal exchange, temperature and salinity are found to occupy a much larger range in values leading to more spice variability. Both cool/fresh and warm/salty anomalies are observed indicating intrusions from both sides of the major frontal structure of the ACC.

The spice anomaly variance, which is calculated at every 1° of longitude, is interpolated along each streamline (Fig. 5a). Patterns in cross-frontal exchange observed in Fig. 4 are found to be robust along nearly every streamline. Namely, spice variance is low upstream from, and in proximity to, the ridge system but increases almost as soon as the streamlines propagate off the topography. The northwest-to-southeast step-like geometry of the ridge system is reflected in the standing meander as the northernmost streamlines (13–15 m^2 s^{-2}) are the first to propagate off the topography, destabilize, and exhibit evidence of enhanced cross-frontal exchange. Additionally, the magnitude of spice variance is largest in these northernmost streamlines of the ACC and decreases poleward, with a slight increase again in the southernmost streamline (6 m^2 s^{-2}). The elevated values of spice variance along the northernmost ACC streamlines are attributed to a larger contrast in water mass properties.

To remove this impact and compare along-streamline patterns, spice anomaly variance is normalized by the largest value along each streamline in Fig. 5b. The value of normalized spice variance is then taken at every 1° longitude point and plotted in Fig. 5c for each streamline. Because these values range between 0 and 1, each streamline is offset to qualitatively compare along-stream patterns. These diagnostics reveal that cross-frontal exchange is elevated over a relatively short longitudinal distance. Spice variance peaks just after the streamlines propagate off the topography (Fig. 5c: black line) and then quickly decreases again further downstream.

Brought to you by MBL/WHOI Library | Unauthenticated | Downloaded 05/27/25 11:50 AM UTC

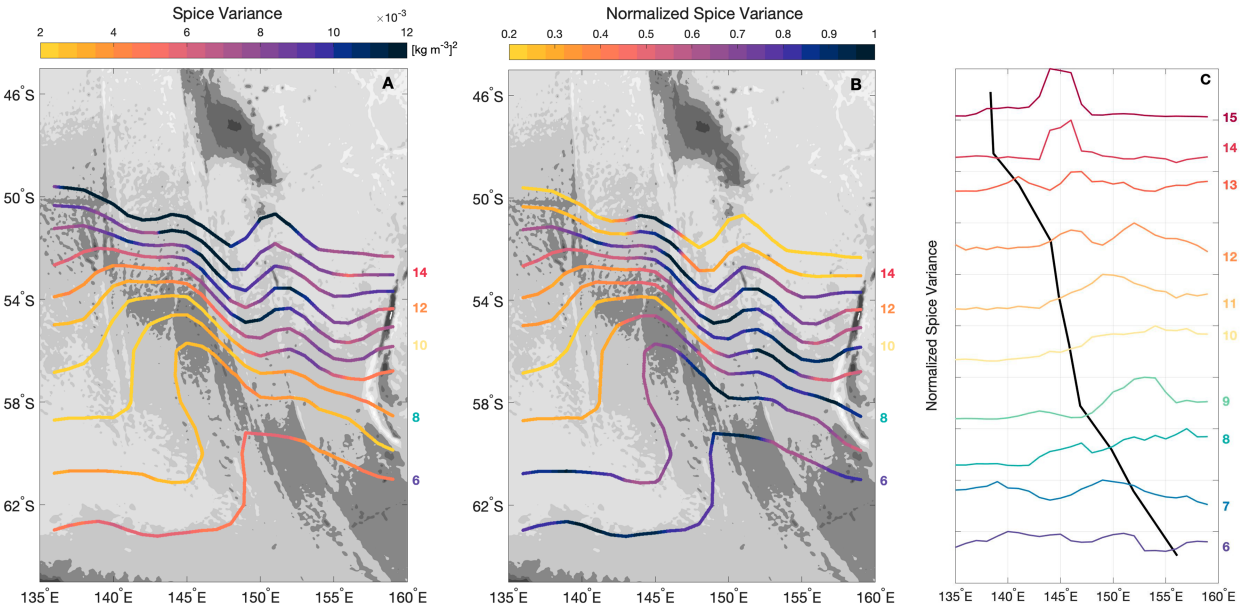


FIG. 5. (a) Total spice anomaly variance along streamlines of the ACC contoured on top of bathymetry in gray. (b) Total spice anomaly variance normalized by the largest spice variance value on each streamline. (c) Normalized spice anomaly variance at each 1° longitude point and plotted along each streamline. The geopotential streamline is labeled on the right-hand side of each panel. The color of the label corresponds to the geopotential contour with purple and blue representing the southernmost streamlines (6 and 7 $m^2\ s^{-2}$), while the red represents the northernmost streamlines (13–15 $m^2\ s^{-2}$). The black line represents the mean position of the ridge.

Additionally, spice variance peaks progressively downstream along each poleward streamline (Fig. 5c). This pattern illustrates a north-to-south handoff of fluid across nearly the full breadth of the ACC. This is likely a consequence of the geometry of the ridge system, angled such that the northernmost streamlines encounter the ridge and destabilize first, followed by the interior streamlines and eventually the southernmost streamlines. These southernmost streamlines (6 and 7 $m^2\ s^{-2}$) have nearly constant spice variance throughout the SEIR region and do not exhibit the characteristic downstream peak. This may be attributable to the topography but could also be a consequence of our choice to exclude the mixed layer from this analysis. As eddies are preferentially moving fluid poleward and upward across the ACC, exchange may be occurring too close to the surface for us to detect using this analysis.

The total spice anomaly variance at each 1° longitude point along streamlines was used to diagnose the above results. A spice anomaly variance profile (Fig. 2e) can also be obtained by calculating the spice variance on isopycnal (or depth) layers to identify the density (or depth) at which maximum exchange occurs. In Fig. 6, spice anomaly variance profiles, in density (top) and depth (bottom) spice, are plotted against longitude at every 1° along a number of geopotential height contours. On the rightmost side of Fig. 6, spice anomaly variance is averaged in longitude to obtain a single representative spice anomaly profile for each geopotential streamline. Figure 6 illustrates that spice variance peaks below the mixed layer but can extend throughout the top of the water column. Additionally, in density space, maximum spice variance is observed to occur on denser isopycnals moving poleward across the ACC (Fig. 6a). In the northernmost streamlines (13–15 $m^2\ s^{-2}$), the largest values of spice variance are confined to a small density range of about 26.9 ± 0.1 kg m^{-3}. The more central streamlines (8–12 $m^2\ s^{-2}$) are characterized by peaks between 27 and 27.2 kg m^{-3}. The southernmost streamlines (6 and 7 $m^2\ s^{-2}$) also have distinct peaks at 27.5 and 27.35 $m^2\ s^{-2}$ but exhibit the smallest magnitude of spice variance. In depth space, maximum variance occurs at shallower depths moving poleward across the ACC (Fig. 6b). These patterns reflect the poleward shoaling pycnoline structure and illustrate patterns of exchange that occur just below the mixed layer.

b. *Eddy diffusivity*

Horizontal eddy diffusivity is the product of a mixing length scale L_{mix} and an eddy velocity scale U_e. The eddy mixing length scale is interpreted as the distance over which fluid properties are transported by turbulent eddies during eddy stirring before complete, irreversible mixing occurs. Increased L_{mix} suggests an eddy field that can transport fluid parcels over larger distances. Here, eddy mixing length scale (Fig. 7a) is relatively high upstream from the ridge system, just before streamlines pinch together when they encounter the topography. However, on the topography and just as streamlines propagate off the topography, L_{mix} sharply decreases to its lowest values within the study domain. Further downstream, L_{mix} increases to maximum values of around 200 km between the crest and trough of the standing meander (149°–153°E) before decreasing again downstream from the trough axis (note that meander crests are associated with anticyclonic curvature and are therefore always poleward deviations in a

Brought to you by MBL/WHOI Library | Unauthenticated | Downloaded 05/27/25 11:50 AM UTC

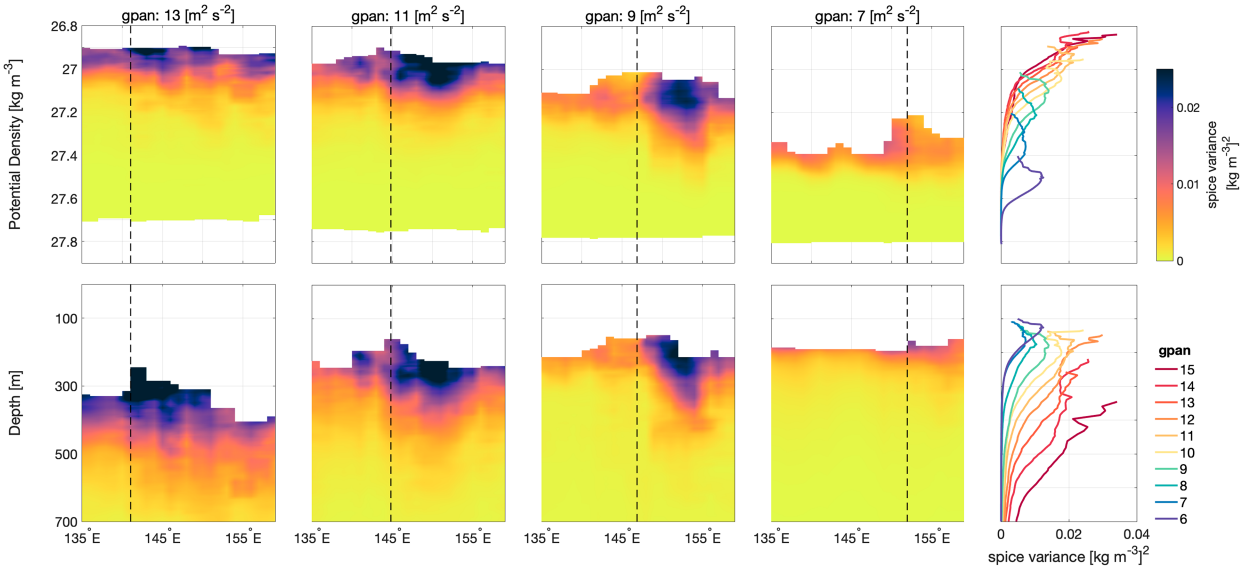


FIG. 6. Spice variance in (top) density space and (bottom) depth space vs longitude along geopotential streamlines 13, 11, 9, and 7 $m^2\ s^{-2}$ (from left to right, respectively). Dashed lines represent the mean position of the ridge at that streamline. On the far right, mean spice variance profiles are averaged along each geopotential height contour. Red profiles indicate equatorward streamlines, and the transition to poleward streamlines is indicated in the blues and purples.

zonal current). These downstream values are of similar magnitude to those observed upstream from the topography.

We briefly consider the property, spice root-mean-square [Eq. (1) numerator] or background spice gradient [Eq. (1) denominator] that primarily controls observed patterns of mixing length; however, we caution that this discussion is nuanced as both properties will change in both space and time. Regardless, our interpretation is that in both the upstream and downstream regions, patterns of L_{mix} seem to be equally as controlled by the spice root-mean-square value as by the background spice gradient. In other words, a relatively small change in either value could result with a fairly significant change in the resulting mixing length scale. In comparison, near the topography, background spice gradients are exceptionally strong as streamlines pinch together, resulting in the lowest values of L_{mix} within our domain. Therefore, near the topography, patterns L_{mix} are more heavily controlled by background gradients. Even a significant change in the spice root-mean-square would not result in a strong change to mixing length. In the meander, background spice gradients decrease while spice root-mean-square values remain high or increase further, resulting in high values of L_{mix}. Here, patterns of L_{mix} are therefore more heavily controlled by spice root-mean-square values, and a large change in the background gradient would not have a strong impact on patterns of mixing length.

The eddy velocity scale is interpreted as the strength of turbulent eddies such that an increase in U_e represents an increase in the speed at which eddies are acting to move fluid parcels and homogenize the tracer field. Here, the eddy velocity scale (Fig. 7b) is exceptionally low upstream from and over the ridge. However, when streamlines propagate off the topography and isopycnals become unstable, U_e begins to increase. It continues to increase throughout the standing meander and more slowly decreases further downstream. The resulting eddy diffusivity κc_e^{-1} illustrates a very clear pattern. Diffusivity is relatively low upstream from the ridge system and uniformly decreases to a domain minimum as streamlines trend southeastward off the topography. It then intensifies by about an order of magnitude leading into the standing meander, peaking to a maximum between the crest and trough of the standing meander. Diffusivity then quickly decreases by a factor of 2–3 further downstream from the meander trough (Fig. 7c). Maximum values, which will be on the order of about 8–10 $\times$ 10^3 $m^2\ s^{-1}$ when a typical mixing coefficient is accounted for ($c_e = 0.1$), are characteristically confined to the notably short distance between the crest and trough of the meander.

5. Discussion

a. *Comparison of diffusivity estimates*

Quantifying the transport of climate relevant tracers within ocean and climate models is particularly important in the Southern Ocean, where isopycnal eddy stirring plays a significant role in large-scale circulation. This quantification, however, depends on an accurate representation of eddy diffusivity. Here, we have shown maximum values of eddy diffusivity, estimated from a mixing length framework, on the order of 8–10 $\times$ 10^3 $m^2\ s^{-1}$ characteristically confined between the crest and trough of the standing meander formed in the lee of the Southeast Indian Ridge. Here, we will put these findings in context of previous studies and discuss the implications for modeling and predicting future change.

Brought to you by MBL/WHOI Library | Unauthenticated | Downloaded 05/27/25 11:50 AM UTC

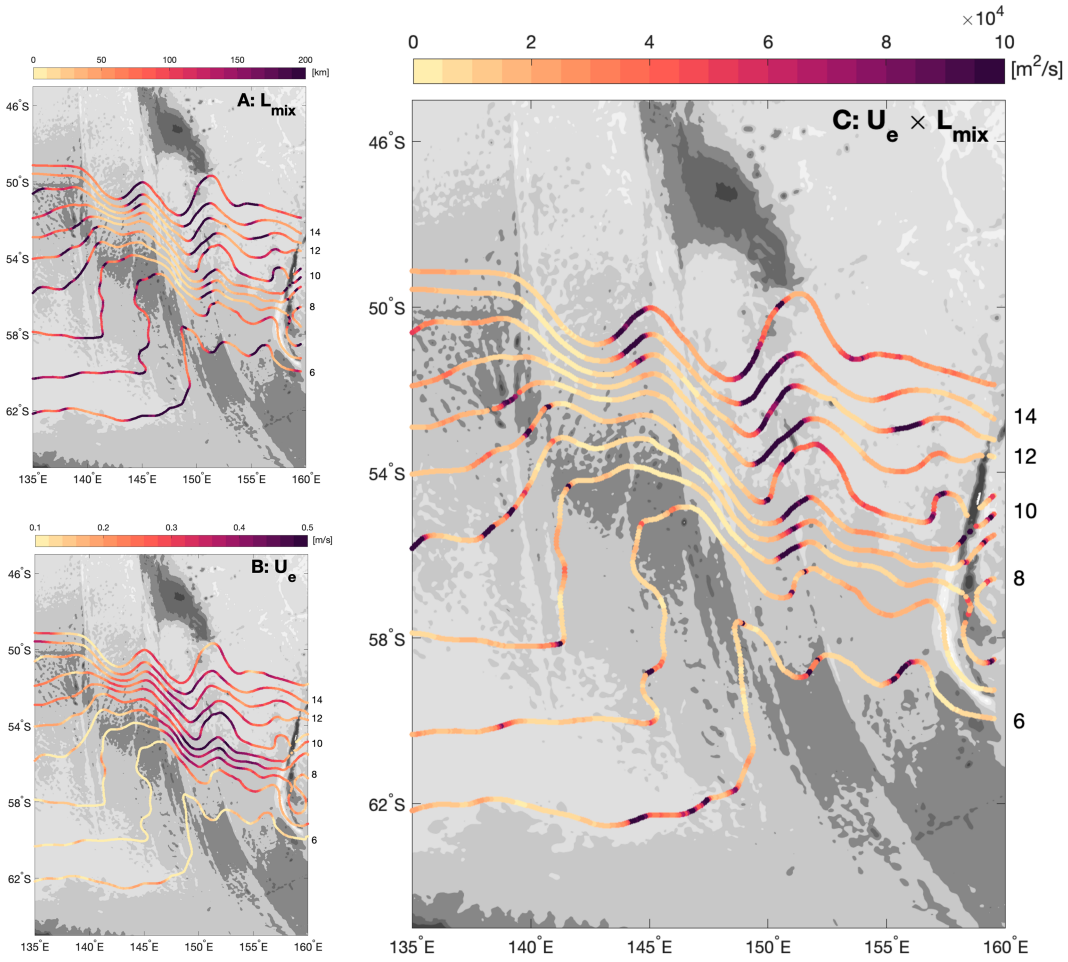


FIG. 7. Bottom topography under (a) eddy mixing length scale, (b) eddy velocity scale, and (c) eddy diffusivity estimate κc_e^{-1}. Parameters are mapped to geopotential streamlines along the isopycnal of peak exchange as determined from Fig. 6. Geopotential contours are calculated from the GLORYS product and labeled on the right-hand side in units of ($m^2\ s^{-2}$).

This work is primarily built upon two previous studies, Cole et al. (2015) and Naveira Garabato et al. (2011), which both use hydrographic variability and a mixing length framework to estimate eddy diffusivity. Cole et al. (2015) shows elevated values of eddy diffusivity, on the order of 5–8 $\times$ 10^3 $m^2\ s^{-1}$ at the base of the mixed layer near the Southeast Indian Ridge. Comparable values were found in other topographic regions around the Southern Ocean. Naveira Garabato et al. (2011) find values exceeding 2×10^3 $m^2\ s^{-1}$ (when accounting for a mixing coefficient of $c_e = 0.1$) extending from below the mixed layer to about 2000-m depth, most commonly associated with the Subantarctic Front. These estimates, however, were confined to synoptic CTD sections which often did not traverse through these strong eddy stirring regimes.

A number of other studies have used observations to quantify eddy diffusivity in the Southern Ocean. Closely related to this work, both Roach et al. (2016) and Chapman and Sallée (2017) use Argo floats to get along-stream estimates spanning the entire ACC. While Roach et al. (2016) use the dispersion of floats at their parking depth and Chapman and Sallée (2017) use dynamic height variability on the 27.9 kg m^{-3} isopycnal, both identify diffusivity peaks on the order of 1–3 $\times$ 10^3 $m^2\ s^{-1}$ associated with each topographic ridge system. Consistent with these estimates, Balwada et al. (2016) and LaCasce et al. (2014) show that diffusivity is on the order of 10^3 $m^2\ s^{-1}$ upstream from Drake Passage using the dispersion of RAFOS floats. Peak diffusivity observed here is on the higher end of previously reported values in the Southern Ocean; however, given the higher resolution and range in mixing coefficients, we believe our estimate is within reason.

The most striking feature of our diffusivity estimate is not the magnitude, which can be dependent on methodology and the value of the mixing coefficient used, but the distinct pattern of peak diffusivity leading into the trough of the meander for all streamlines of the ACC. This pattern is markedly similar to the diffusivity pattern found by Abernathey and Cessi (2014) who use a numerical simulation to interpret the impact of topography on the efficiency of baroclinic conversion into eddy potential energy. The influence of topography on

Brought to you by MBL/WHOI Library | Unauthenticated | Downloaded 05/27/25 11:50 AM UTC

idealized streamlines results in a standing meander nearly identical to that in the SEIR region and a downgradient divergent flux in the lee of the ridge. A resulting eddy diffusivity, with maximum values exceeding 5×10^3 m^2 s^{-1}, is found to be similarly localized between the crest and trough of the standing meander with peak values just downstream from the first crest. Additionally, diffusivity is shown to be significantly suppressed elsewhere along streamlines, especially over the ridge system. This result is in very close agreement to patterns observed in Fig. 7.

Abernathey et al. (2010) suggest that this highly localized nature of eddy diffusivity and baroclinic conversion can be attributed to the local kinematics of eddy growth which depends not only on horizontal buoyancy gradients but additionally on the zonal flow which can propagate disturbances away from baroclinically unstable regions. They argue that baroclinic conversion of energy begins to occur immediately downstream from the ridge, but perturbations can then be quickly advected downstream. This results in maximum diffusivity values found downstream from peak baroclinic conversion. They also suggest that the localization of these eddy fluxes increases as a function of the magnitude of the wind and amplitude of the stationary meander. As the magnitude of Southern Ocean winds has increased in response to anthropogenic warming, the observed localized nature of eddy diffusivity could become increasingly important to understand as we attempt to parameterize these processes in coupled ocean and climate models (Yin 2005; Fyfe and Saenko 2006).

b. *Comparison with altimetry proxies*

A number of studies have defined simple altimetric-based proxies to quantify the impact of the mesoscale eddy field in the ACC. On a circumpolar scale, Sallée et al. (2008) find a strong correlation between eddy kinetic energy (EKE) and cross-stream eddy diffusivity using simulated Lagrangian surface drifters released within satellite-derived velocity fields. To identify large-scale spatial distributions of mixing regimes, this type of simple parameterization may be sufficient; however, more recent work has suggested that EKE may not be the most accurate metric to use as a proxy for baroclinically unstable regions.

Spatial and temporal trends in eddy heat flux and eddy diffusivity have been shown to not always reflect those of EKE (e.g., Shuckburgh et al. 2009). Numerical simulations by Chapman et al. (2015) suggest that baroclinic conversion of available mean potential energy to eddy potential energy occurs immediately downstream from the ridge, while EKE peaks further downstream. They argue that the along-stream growth in EKE more accurately represents the spatial patterns of baroclinic conversion. Using observations from Drake Passage, Foppert et al. (2017) also illustrate a spatial offset between maximum eddy heat fluxes and EKE. In contrast, they argue that sea surface height standard deviation (H^*) is a superior proxy for baroclinic instability as the conversion to eddy potential energy is achieved through the downgradient flux of heat across the background temperature (or sea surface height in the strongly baroclinic environment) gradient.

Here, we compare observed patterns of eddy diffusivity in the SEIR region to altimetry-derived patterns in sea surface height standard deviation, EKE, and the zonal gradient in EKE. Consistent with Foppert et al. (2017), a spatial offset between sea surface height standard deviation and EKE is observed (Figs. 8a,b, respectively). Maximum values of sea surface height standard deviation appear to be confined to the crest of the standing meander, while EKE grows throughout the first wavelength (145°–152°E) and remains high further downstream. The spatial offset of peak H^* and EKE is about 1°–2° of longitude, consistent with observations in Drake Passage (Foppert et al. 2017). Diffusivity, however, is found to spatially align most closely with the zonal growth of eddy kinetic energy, between maximum values in H^* and EKE (Fig. 8c).

This is consistent with numerical simulations by Chapman et al. (2015). They suggest that eddies grow in the lee of the ridge by extracting available potential energy from the mean field and converting it to eddy kinetic energy. Subsequent to this initial extraction, an energy flux acts to transport energy further downstream to maintain elevated values of EKE further downstream from the baroclinically unstable regions. Here, we suggest a slightly modified system that overlaps with both Abernathey and Cessi (2014) and Chapman et al. (2015). The standing meander is formed in the immediate lee of the ridge, tightening horizontal buoyancy gradients and resulting in strong baroclinic conversion of energy between mean and eddy reservoirs. This baroclinic conversion is associated with maximum values of sea surface height standard deviation. The strong flow, however, sweeps perturbations downstream sustaining peak values of diffusivity slightly downstream, between the crest and trough of the meander. Eddy kinetic energy is growing and being fluxed in the along-stream direction which is sustaining elevated values further downstream from the standing meander. This results in peak values of diffusivity that aligns with the along-stream growth of EKE and occurs further downstream from maximum sea surface height standard deviation.

c. *Vertical scales of intrusions*

We propose an along-stream evolution of cross-frontal intrusions that may be described as follows. Water parcel exchange across fronts of the ACC is driven by baroclinic instability. Previous work in the Drake Passage showed that exchange is driven by energetic abyssal eddies that develop jointly with upper meanders, and the ensuing cross-front current components extend through the full water column (Watts et al. 2016). Initial hydrographic anomalies have vertical scales comparable to the permanent pycnocline, as would occur from lateral displacement by a nearly depth-independent cross-frontal component of current. Fluid does not immediately become homogenized into the mean. In the downstream direction, flow becomes filamented as anomalies, that are created by cross-frontal exchange and are nearly depth independent, are stretched and folded across the sheared mesoscale

Brought to you by MBL/WHOI Library | Unauthenticated | Downloaded 05/27/25 11:50 AM UTC

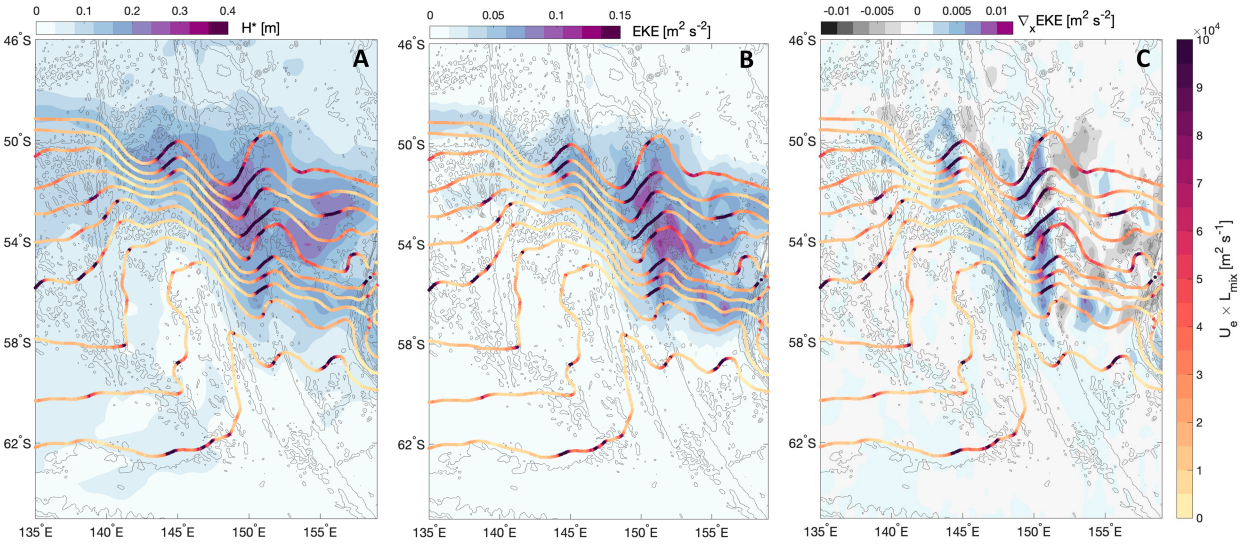


FIG. 8. Observed eddy diffusivity along geopotential streamlines overlaid on (a) sea surface height standard deviation (H^*), (b) eddy kinetic energy, and (c) zonal gradient in eddy kinetic energy. Note that positive zonal EKE gradients, plotted in blue shades, tend to align with high eddy diffusivity, while negative EKE gradients, in grayscale, align with lower diffusivity. Bottom topography is contoured every 1000 m in light gray.

eddy field. This results in a reduction of the vertical scale of the anomaly and a downstream cascade of the vertical wavenumber.

This transfer of variance to smaller scales can be evaluated by an along-stream, variance-preserving, vertical wavenumber spectrum of spice anomaly profiles (Fig. 9). A power spectral density using the Welch averaged modified periodogram method with a Hanning window taper is used. The top 150 m of each profile is removed to minimize the influence of the mixed layer. Various mixed-layer thresholds were tested with very little impact on the results shown. Spectra are calculated in depth space, after a mean spice profile is removed, along each longitudinal point of geopotential streamlines, using the same 3° sliding window as before. This ensures each spectrum is calculated and ensemble averaged over 50–200 profiles depending upon data density within each longitudinal bin.

A general pattern reflecting a downstream cascade in the vertical scale of anomalies is present across streamlines in the along-stream wavenumber spectra. The most striking example is along the Polar Front (Fig. 9d), where vertical anomalies have a maximum at 800 m at their formation, located from 150° to 155°E. Further downstream, the filaments that originally formed with a large vertical scale comparable to the pycnocline have been strained or broken into smaller vertical scales of 100–300 m. Other streamlines (Figs. 9a–c) reflect a similar pattern albeit more subtle. This pattern is consistent with nearly depth-independent cross-stream exchange at active baroclinic instability centers followed immediately by mesoscale filamentation of the flow that aids in homogenization of hydrographic anomalies into the mean. More work is required to address this vertical downstream cascade of spice variance anomalies.

6. Summary and conclusions

In this study, cross-frontal exchange facilitated by the mesoscale eddy field is characterized in the Southeast Indian Ridge (SEIR) system of the Southern Ocean. Over a decade of Argo profiles in the region are mapped to ACC streamlines and used to identify along-stream patterns of hydrographic variability. We argue this variability, namely, the spice anomaly variance, is a reliable proxy for the exchange of particles across fronts, and the methodology provides a high-resolution, three-dimensional assessment of along-stream patterns. We focus on the SEIR region because it has been identified as a hotspot for cross-frontal exchange (Sallée et al. 2011; Thompson and Sallée 2012; Thompson and Garabato 2014; Meijer et al. 2022). Additionally, it is a relatively understudied and underobserved topographic region of the Southern Ocean.

Cross-frontal exchange is found to be elevated downstream from the ridge system in nearly all ACC streamlines. Maximum exchange occurs along the equatorward flank of the ACC and decreases along each poleward streamline. Spice anomaly variance is normalized along each streamline to reveal a distinct pattern in the SEIR region: cross-frontal exchange peaks progressively downstream along each poleward streamline suggestive of a north-to-south handoff of fluid parcels and their associated properties across nearly the full breadth of the ACC. This suggests the ridge system is effective at producing cross-frontal exchange and plays a critical role in the Southern Ocean overturning circulation.

This analysis lends itself to a local, high-resolution, hydrographic-variability-based estimate of eddy diffusivity in the SEIR region. Within the mixing length framework, cross-stream eddy diffusivity relates the background mean tracer field (obtained from GLORYS) to the observed departure from that mean (Argo). Eddy diffusivity is found to be relatively low upstream from the ridge system and decreases as streamlines encounter the topography. Diffusivity then

Brought to you by MBL/WHOI Library | Unauthenticated | Downloaded 05/27/25 11:50 AM UTC

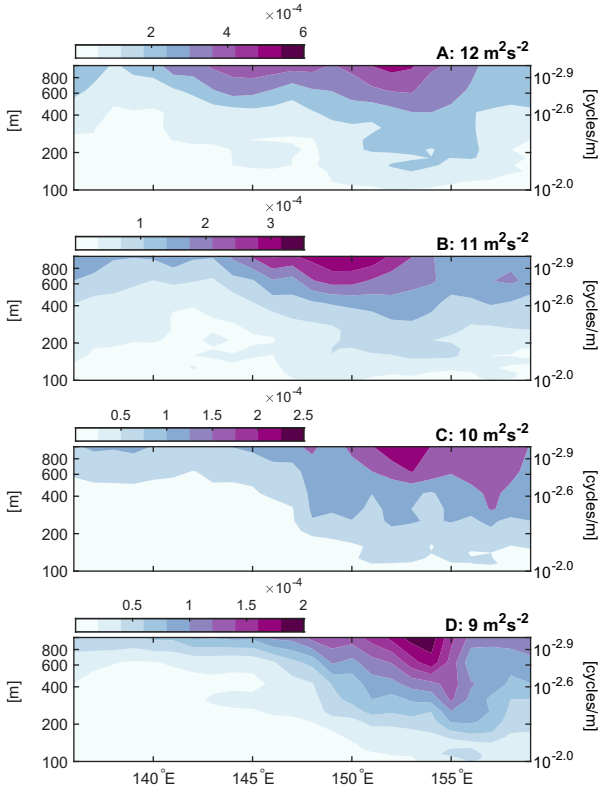


FIG. 9. Along-stream vertical spice anomaly wavenumber spectra on geopotential streamlines from (a) 12 $m^2 s^{-2}$ to (d) 9 $m^2 s^{-2}$. The vertical wavenumber of intrusions is given on the right axis. The corresponding vertical scale k^{-1} is on the left axis. Note that the colorbars change to reveal the weaker spice variance along southern streamlines.

intensifies by about an order of magnitude leading into the standing meander but quickly decreases (by a factor of 2–3) again further downstream. Maximum diffusivity is confined to a notably short distance between the crest and trough of the meander, a pattern strikingly similar to idealized model simulations (Abernathey and Cessi 2014).

The observed patterns of eddy diffusivity are compared to altimetric-based parameters, eddy kinetic energy and sea surface height standard deviation (H^*). Both have previously been proposed as proxies for diffusivity (Sallée et al. 2008) and eddy heat flux (Foppert et al. 2017), respectively. As documented in other topographic Southern Ocean hotspots, a spatial offset exists between H^* and EKE, with EKE peaking further downstream (Chang and Orlanski 1993; Chapman et al. 2015; Foppert et al. 2017). Neither parameter, however, appears to have a stronger spatial correlation to eddy diffusivity which is found to peak between H^* and EKE maxima. Instead, diffusivity is found to align closely with the along-stream gradient of EKE, peaking where the growth of EKE is the largest.

Finally, we explore the transfer of variance from large to small scales in response to the intensification of the mesoscale eddy field as indicated by the along-stream increase in EKE. This is evaluated using a series of variance-preserving wavenumber spectra on spice anomaly profiles. We find a general pattern of spectra evolving to higher wavenumbers downstream of the peak exchange, in accord with a downstream cascade to smaller vertical scales. The most striking example is along the Polar Front, where anomalies have a vertical extent of the pycnocline, 800 m, where exchange is initiated but reduce to 100–300 m further downstream.

This work provides high-resolution insight into patterns of cross-frontal exchange and eddy diffusivity in the SEIR region of the Southern Ocean. These results have broad implications for the ways in which eddy-driven processes are parameterized in ocean and climate models, especially under future anthropogenic warming and associated changes in the wind forcing.

Acknowledgments. The authors thank Kurt Polzin for several thoughtful discussions regarding the analysis and interpretation of results presented here. The authors would also like to extend sincere gratitude to the three reviewers for their insightful comments and suggestions, which significantly improved the quality and clarity of this manuscript. Funding for this project was provided by the National Science Foundation Grant OCE-2023306.

Data availability statement. These data were collected and made freely available by the International Argo Program and the national programs that contribute to it (https://argo.ucsd.edu, https://www.ocean-ops.org). The Argo Program is part of the Global Ocean Observing System. The GLORYS reanalysis product is a joint effort between Mercator Ocean and the CORIOLIS data center. Data are made freely available by the Copernicus Marine Environment Monitoring Service found at: https://data.marine.copernicus.eu/product/GLOBAL_MULTIYEAR_PHY_001_030/description. The mapped altimeter SSH product can be found at: https://data.marine.copernicus.eu/product/SEALEVEL_GLO_PHY_L4_MY_008_047/services.

REFERENCES

Abernathey, R., and P. Cessi, 2014: Topographic enhancement of eddy efficiency in baroclinic equilibration. *J. Phys. Oceanogr.*, **44**, 2107–2126, https://doi.org/10.1175/JPO-D-14-0014.1.

——, J. Marshall, M. Mazloff, and E. Shuckburgh, 2010: Enhancement of mesoscale eddy stirring at steering levels in the Southern Ocean. *J. Phys. Oceanogr.*, **40**, 170–184, https://doi.org/10.1175/2009JPO4201.1.

Argo, 2000: Argo float data and metadata from Global Data Assembly Centre (Argo GDAC). SEANOE, accessed 15 December 2022, https://doi.org/10.17882/42182.

Balwada, D., K. G. Speer, J. H. LaCasce, W. B. Owens, J. Marshall, and R. Ferrari, 2016: Circulation and stirring in the southeast Pacific Ocean and the Scotia Sea sectors of the Antarctic Circumpolar Current. *J. Phys. Oceanogr.*, **46**, 2005–2027, https://doi.org/10.1175/JPO-D-15-0207.1.

Brady, R. X., M. E. Maltrud, P. J. Wolfram, H. F. Drake, and N. S. Lovenduski, 2021: The influence of ocean topography on the upwelling of carbon in the Southern Ocean.

Brought to you by MBL/WHOI Library | Unauthenticated | Downloaded 05/27/25 11:50 AM UTC

Geophys. Res. Lett., **48**, e2021GL095088, https://doi.org/10.1029/2021GL095088.

Bryan, K., and L. J. Lewis, 1979: A water mass model of the world ocean. *J. Geophys. Res.*, **84**, 2503–2517, https://doi.org/10.1029/JC084iC05p02503.

Chang, E. K. M., and I. Orlanski, 1993: On the dynamics of a storm track. *J. Atmos. Sci.*, **50**, 999–1015, https://doi.org/10.1175/1520-0469(1993)050<0999:OTDOAS>2.0.CO;2.

Chapman, C., and J.-B. Sallée, 2017: Isopycnal mixing suppression by the Antarctic Circumpolar Current and the Southern Ocean meridional overturning circulation. *J. Phys. Oceanogr.*, **47**, 2023–2045, https://doi.org/10.1175/JPO-D-16-0263.1.

Chapman, C. C., A. M. Hogg, A. E. Kiss, and S. R. Rintoul, 2015: The dynamics of Southern Ocean storm tracks. *J. Phys. Oceanogr.*, **45**, 884–903, https://doi.org/10.1175/JPO-D-14-0075.1.

Cole, S. T., C. Wortham, E. Kunze, and W. B. Owens, 2015: Eddy stirring and horizontal diffusivity from Argo float observations: Geographic and depth variability. *Geophys. Res. Lett.*, **42**, 3989–3997, https://doi.org/10.1002/2015GL063827.

Deacon, G. E. R., 1937: The hydrology of the Southern Ocean. *Discovery Rep.*, **15**, 3–122.

Dufour, C. O., and Coauthors, 2015: Role of mesoscale eddies in cross-frontal transport of heat and biogeochemical tracers in the Southern Ocean. *J. Phys. Oceanogr.*, **45**, 3057–3081, https://doi.org/10.1175/JPO-D-14-0240.1.

Ferrari, R., and M. Nikurashin, 2010: Suppression of eddy diffusivity across jets in the Southern Ocean. *J. Phys. Oceanogr.*, **40**, 1501–1519, https://doi.org/10.1175/2010JPO4278.1.

Foppert, A., K. A. Donohue, D. R. Watts, and K. L. Tracey, 2017: Eddy heat flux across the Antarctic Circumpolar Current estimated from sea surface height standard deviation. *J. Geophys. Res. Oceans*, **122**, 6947–6964, https://doi.org/10.1002/2017JC012837.

Fyfe, J. C., and O. A. Saenko, 2006: Simulated changes in the extratropical Southern Hemisphere winds and currents. *Geophys. Res. Lett.*, **33**, L06701, https://doi.org/10.1029/2005GL025332.

Gent, P. R., and J. C. Mcwilliams, 1990: Isopycnal mixing in ocean circulation models. *J. Phys. Oceanogr.*, **20**, 150–155, https://doi.org/10.1175/1520-0485(1990)020<0150:IMIOCM>2.0.CO;2.

Holte, J., and L. Talley, 2009: A new algorithm for finding mixed layer depths with applications to Argo data and Subantarctic mode water formation. *J. Atmos. Oceanic Technol.*, **26**, 1920–1939, https://doi.org/10.1175/2009JTECHO543.1.

Klocker, A., R. Ferrari, J. H. LaCasce, and S. T. Merrifield, 2012: Reconciling float-based and tracer-based estimates of lateral diffusivities. *J. Mar. Res.*, **70**, 569–602, https://doi.org/10.1357/002224012805262743.

LaCasce, J. H., R. Ferrari, J. Marshall, R. Tulloch, D. Balwada, and K. Speer, 2014: Float-derived isopycnal diffusivities in the DIMES experiment. *J. Phys. Oceanogr.*, **44**, 764–780, https://doi.org/10.1175/JPO-D-13-0175.1.

Lumpkin, R., and K. Speer, 2007: Global ocean meridional overturning. *J. Phys. Oceanogr.*, **37**, 2550–2562, https://doi.org/10.1175/JPO3130.1.

Marshall, J., and K. Speer, 2012: Closure of the meridional overturning circulation through Southern Ocean upwelling. *Nat. Geosci.*, **5**, 171–180, https://doi.org/10.1038/ngeo1391.

McDougall, T. J., and O. A. Krzysik, 2015: Spiciness. *J. Mar. Res.*, **73**, 141–152, https://doi.org/10.1357/002224015816665589.

Meijer, J. J., H. E. Phillips, N. L. Bindoff, S. R. Rintoul, and A. Foppert, 2022: Dynamics of a standing meander of the subantarctic front diagnosed from satellite altimetry and along-stream anomalies of temperature and salinity. *J. Phys. Oceanogr.*, **52**, 1073–1089, https://doi.org/10.1175/JPO-D-21-0049.1.

Naveira Garabato, A. C., R. Ferrari, and K. L. Polzin, 2011: Eddy stirring in the Southern Ocean. *J. Geophys. Res.*, **116**, C09019, https://doi.org/10.1029/2010JC006818.

Peña-Molino, B., S. R. Rintoul, and M. R. Mazloff, 2014: Barotropic and baroclinic contributions to along-stream and across-stream transport in the Antarctic Circumpolar Current. *J. Geophys. Res. Oceans*, **119**, 8011–8028, https://doi.org/10.1002/2014JC010020.

Phillips, H. E., and S. R. Rintoul, 2000: Eddy variability and energetics from direct current measurements in the Antarctic Circumpolar Current South of Australia. *J. Phys. Oceanogr.*, **30**, 3050–3076, https://doi.org/10.1175/1520-0485(2000)030<3050:EVAEFD>2.0.CO;2.

Pond, S., and G. L. Pickard, 1983: *Introductory Dynamical Oceanography*. Pergamon Press, 329 pp.

Rintoul, S. R., 2018: The global influence of localized dynamics in the Southern Ocean. *Nature*, **558**, 209–218, https://doi.org/10.1038/s41586-018-0182-3.

Roach, C. J., D. Balwada, and K. Speer, 2016: Horizontal mixing in the Southern Ocean from Argo float trajectories. *J. Geophys. Res. Oceans*, **121**, 5570–5586, https://doi.org/10.1002/2015JC011440.

Sallée, J. B., K. Speer, R. Morrow, and R. Lumpkin, 2008: An estimate of Lagrangian eddy statistics and diffusion in the mixed layer of the Southern Ocean. *J. Mar. Res.*, **66**, 441–463, https://doi.org/10.1357/002224008787157458.

——, ——, and S. R. Rintoul, 2011: Mean-flow and topographic control on surface eddy-mixing in the Southern Ocean. *J. Mar. Res.*, **69**, 753–777, https://doi.org/10.1357/002224011799849408.

Shuckburgh, E., H. Jones, J. Marshall, and C. Hill, 2009: Understanding the regional variability of eddy diffusivity in the Pacific sector of the Southern Ocean. *J. Phys. Oceanogr.*, **39**, 2011–2023, https://doi.org/10.1175/2009JPO4115.1.

Sloyan, B. M., and S. R. Rintoul, 2001: The Southern Ocean limb of the global deep overturning circulation. *J. Phys. Oceanogr.*, **31**, 143–173, https://doi.org/10.1175/1520-0485(2001)031<0143:TSOLOT>2.0.CO;2.

Speer, K., S. R. Rintoul, and B. Sloyan, 2000: The diabatic Deacon cell. *J. Phys. Oceanogr.*, **30**, 3212–3222, https://doi.org/10.1175/1520-0485(2000)030<3212:TDDC>2.0.CO;2.

Tamsitt, V., and Coauthors, 2017: Spiraling pathways of global deep waters to the surface of the Southern Ocean. *Nat. Commun.*, **8**, 172, https://doi.org/10.1038/s41467-017-00197-0.

Thompson, A. F., and J.-B. Sallée, 2012: Jets and topography: Jet transitions and the impact on transport in the Antarctic Circumpolar Current. *J. Phys. Oceanogr.*, **42**, 956–972, https://doi.org/10.1175/JPO-D-11-0135.1.

——, and A. C. N. Garabato, 2014: Equilibration of the Antarctic Circumpolar Current by standing meanders. *J. Phys. Oceanogr.*, **44**, 1811–1828, https://doi.org/10.1175/JPO-D-13-0163.1.

Tulloch, R., and Coauthors, 2014: Direct estimate of lateral eddy diffusivity upstream of Drake Passage. *J. Phys. Oceanogr.*, **44**, 2593–2616, https://doi.org/10.1175/JPO-D-13-0120.1.

Watts, D. R., K. L. Tracey, K. A. Donohue, and T. K. Chereskin, 2016: Estimates of eddy heat flux crossing the Antarctic Circumpolar Current from observations in Drake Passage. *J.*

Brought to you by MBL/WHOI Library | Unauthenticated | Downloaded 05/27/25 11:50 AM UTC

Phys. Oceanogr., **46**, 2103–2122, https://doi.org/10.1175/JPO-D-16-0029.1.

Wong, A. P. S., and Coauthors, 2020: Argo data 1999–2019: Two million temperature-salinity profiles and subsurface velocity observations from a global array of profiling floats. *Front. Mar. Sci.*, **7**, 700, https://doi.org/10.3389/fmars.2020.00700.

Yin, J. H., 2005: A consistent poleward shift of the storm tracks in simulations of 21st century climate. *Geophys. Res. Lett.*, **32**, L18701, https://doi.org/10.1029/2005GL023684.

Youngs, M. K., A. F. Thompson, A. Lazar, and K. J. Richards, 2017: ACC meanders, energy transfer, and mixed barotropic–baroclinic instability. *J. Phys. Oceanogr.*, **47**, 1291–1305, https://doi.org/10.1175/JPO-D-16-0160.1.

Brought to you by MBL/WHOI Library | Unauthenticated | Downloaded 05/27/25 11:50 AM UTC